Influence of low-temperature resistivity on fast electron transport in solids: scaling to fast ignition electron beam parameters

P McKenna[1], D A MacLellan[1], N M H Butler[1], R J Dance[1], R J Gray[1], A P L Robinson[2], D Neely[2] and M P Desjarlais[3]

[1] Department of Physics, SUPA, University of Strathclyde, Glasgow G4 0NG, UK
[2] Central Laser Facility, STFC Rutherford Appleton Laboratory, Oxfordshire OX11 0QX, UK
[3] Sandia National Laboratories, PO Box 5800, Albuquerque, NM 87185, USA

E-mail: paul.mckenna@strath.ac.uk

CrossMark

Abstract

The role of low-temperature electrical resistivity in defining the transport properties of mega-Ampere currents of fast (MeV) electrons in solids is investigated using 3D hybrid particle-in-cell (PIC) simulations. By considering resistivity profiles intermediate to the ordered (lattice) and disordered forms of two example materials, lithium and silicon, it is shown that both the magnitude of the resistivity and the shape of the resistivity-temperature profile at low temperatures strongly affect the self-generated resistive magnetic fields and the onset of resistive instabilities, and thus the overall fast electron beam transport pattern. The scaling of these effects to the giga-Ampere electron currents required for the fast ignition scheme for inertial fusion is also explored.

(Some figures may appear in colour only in the online journal)

1. Introduction

Controlling the transport of large (multi-mega-Ampere) currents of fast electrons in dense plasma is important for the many applications of high power laser-solid interactions, including ion acceleration [1, 2] and radiation production [3, 4]. It is also important for the development of the fast ignition (FI) approach to inertial confinement fusion (ICF) [5] in which fast electrons are used to transfer energy from an 'ignition' laser pulse to the compressed Deuterium–Tritium (D–T) fusion fuel. In this scheme, an electron current of the order of giga-Amperes is required to propagate over a distance of 100–200 μm from its source to ignite the compressed fuel. In FI schemes involving a hollow cone (to enable propagation of the ignition laser pulse closer to the compressed fuel) the electrons also propagate through the end wall of the solid-density cone, which is typically 100 μm from the centre of the fuel [6]. The mean electron energy is bound by the requirements for it to be high enough such that the electrons

are not subject to extensive scattering losses and low enough that efficient energy deposition occurs in the hot spot. This in turns sets the peak intensity of the ignition laser pulse to the 10^{20} Wcm^{-2} range, as determined by ponderomotive scaling [7]. The energy of the ignition laser pulse depends not only on the ignition physics, but also on the laser-to-electron energy conversion efficiency and the fast electron transport physics. Reduction of the divergence of the electron beam and the minimisation of transport instabilities leading to energy losses (via Ohmic heating) is important to lower the energy requirements of the ignition laser pulse. The development of radically different beam transport patterns, such as 'annular' beams, can also help to achieve this [8].

Many simulation studies of fast electron transport are based on Spitzer resistivity [9], which is valid only in the limit of substantial heating. However, most laser-solid interaction experiments start with initially cold targets. Given that the design of FI targets is strongly influenced by experimental results and that electron transport codes are benchmarked using these

results, it is important to determine to what extent low temperature effects influence fast electron transport in solids. Through experimentally and numerically investigating electron transport in silicon and different forms of carbon, we have recently shown that the electrical resistivity of a material at temperatures as low as a few eV plays a defining role in the evolution of resistive magnetic fields (B-fields) and thus the fast electron transport physics [10–12]. A picosecond pulse of fast electrons (driven by a picosecond-duration laser pulse) traverses a few hundred-micron-thick target on a timescale in which the background electrons are hot, but the ions are still relatively cold and temporarily retain their lattice structure. The energy coupling from background electrons to ions typically requires timescales from several picoseconds to tens of picoseconds depending on the material. The target is in a transient state of warm dense matter (WDM) in this regime. The material lattice structure was shown to define the evolving material electrical resistivity, η, and thus the strength of the resistive B-field and the onset of resistive propagation instabilities [10].

In a follow-on experiment, laser-accelerated protons were used to isochorically preheat targets to induce lattice-melt and the influence of the resulting resistivity gradients on the fast electron transport was investigated [13]. It was shown that tailoring the heating profile enables the resistive magnetic field to be manipulated and thus properties of the fast electron beam to be varied. In related experiments and modelling, it was further shown that a dip in the resistivity-temperature ($\eta - T$) profile of silicon results in an annular fast electron transport pattern [12]. A transition from a Gaussian-like to an annular fast electron beam profile was demonstrated as the peak intensity of the laser pulse was increased from mid-10^{19} to mid-10^{20} Wcm^{-2}. As discussed below, the annular profile results from a reversal in the direction of the resistive magnetic field formed near the envelope of the beam. The potential to control the production and evolution of annular transport patterns could have a significant impact on FI and other applications, and thus motivates further investigation.

In this paper, we report on numerical simulations of the sensitivity of the fast electron beam transport pattern to the shape of the $\eta - T$ profile at temperatures below the Spitzer regime. The profile is varied between limits set by calculations for the ordered and disordered lattice structure cases of two example materials, lithium and silicon, and the resultant changes to the resistive magnetic field and thus fast electron beam transport are investigated. The factors influencing annular fast electron transport in silicon are explored, both for sub-kJ and for FI-relevant laser pulse parameters.

2. Modelling

The ZEPHYROS hybrid-PIC code [14] is used to simulate the 3D relativistic motion of electrons under the influence of self-generated resistive electric and magnetic fields, as well as collisions. In order for the fast electron current to propagate, a spatially coincident and nearly-balancing cold return current must be drawn from the background [15, 16]. The fast electron and cold return current densities are denoted as $\mathbf{j}_f$ and $\mathbf{j}_r$, respectively. The resistive electric field generated (from Ohm's

law) can be estimated as $\mathbf{E} = -\eta\, \mathbf{j}_f$, and thus from Faraday's law the resulting resistive magnetic field (arising due to the fast electrons) can be written as $\dfrac{\partial \mathbf{B}}{\partial t} = \eta\, \nabla \times \mathbf{j}_f + \nabla \eta \times \mathbf{j}_f$, where η is the target resistivity. The $\eta \nabla \times \mathbf{j}_f$ term generates a magnetic field which directs fast electrons into regions of higher $\mathbf{j}_f$, whilst the $\nabla \eta \times \mathbf{j}_f$ term directs fast electrons into regions of higher η. The return current also heats the background plasma, via Ohmic heating, with power density $\mathbf{j}_r \cdot \mathbf{E} \approx \eta j_f^2$. While the background electrons are treated as a fluid, the fast electron population is described kinetically using the Vlasov equation, which is solved via the PIC method. Collisions are included using the Fokker–Planck collisional operators [17], which account for angular fast electron scattering from background ions and electrons, together with drag generated by the background electrons. The temperature is calculated by the energy deposition due to the slowing down of the fast electrons and the Ohmic heating induced by the return current. The electrical resistivity is obtained from tabulated values of $\eta - T$ defined as an input parameter to the code.

The typical grid used for the simulations reported in section 3 is $200\,\mu\text{m} \times 400\,\mu\text{m} \times 400\,\mu\text{m}$, with cell resolution of $\Delta X = \Delta Y = \Delta Z = 0.5\,\mu\text{m}$. The grid size is varied for the simulations in section 4, but the same cell resolution is maintained. The total number of injected macro-particles is 2×10^8 for all simulations. The time step for the simulations in section 3 is 0.2 ps and 4×10^7 macro-particles are injected at each time step up to the 1 ps pulse duration. The simulations for the longer duration pulses in section 4 are performed with 1×10^7 macro-particles injected in 1 ps time steps. The boundaries are transmissive for all simulations, except for the rear boundary for the cases in section 3, which is reflective. This is done to mimic the effects of fast electron reflection in the sheath fields formed at the target rear surface in experiments. However, as the simulation outputs are sampled just after the bulk of the fast electrons have reached the rear boundary, the reflected electrons do not influence the main fast electron transport pattern.

Electrons are injected at $[X, Y, Z] = [0, 0, 0]$, uniformly over a cone with half-angle equal to $50°$ [18]. It is assumed that 30% of the laser pulse energy is converted to fast electrons. The fast electron energies are in the form of an exponential distribution: $\exp(-E_f/kT_f)$, where E_f is the electron kinetic energy and kT_f is the product of Boltzmann's constant and the fast electron temperature. For the laser intensity considered in this work the ponderomotive scaling [7] reproduces experiments and PIC simulations well and is therefore used to determine T_f. The electrons are injected uniformly over the laser pulse duration and with a Gaussian spatial-intensity distribution.

The $\eta - T$ profiles were calculated as outlined in reference [10]. Quantum molecular dynamics (QMD) simulations were performed using the VASP plane-wave density functional theory code, and the atomic configurations sampled as a function of temperature were used in subsequent wide-ranging Kubo–Greenwood resistivity calculations [19, 20]. These calculations were performed for four cases: ordered and disordered lattice structure, for each of lithium (an example low-Z metal) and silicon (an example semiconductor). Additional,
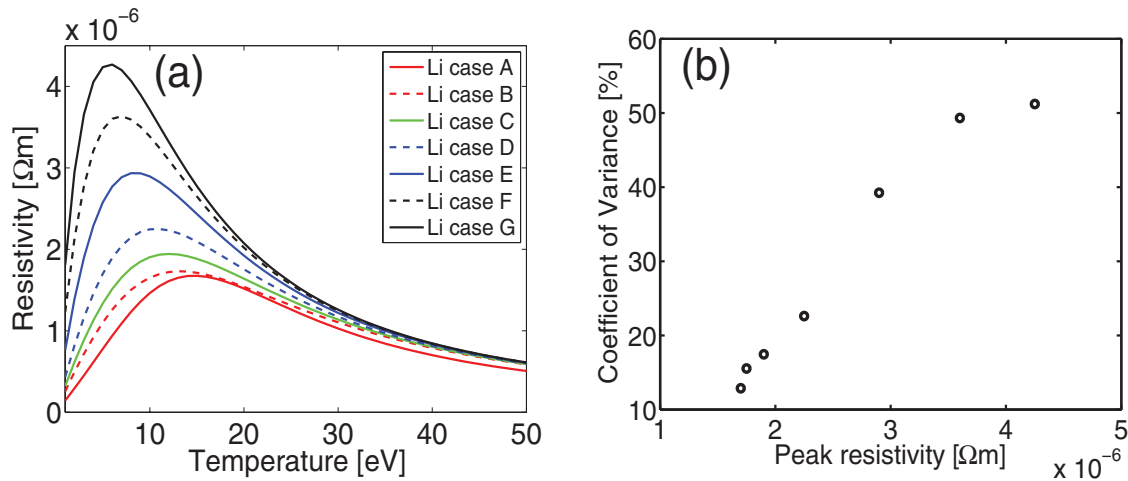
Figure 1. (*a*) Electrical resistivity of lithium as a function of target temperature for an ordered (case A) and a disordered (case G) ion array, based on *ab initio* QMD calculations coupled with the Kubo–Greenwood equation [10]. Cases B–F correspond to intermediate devised $\eta - T$ profiles, used to enable fast electron beam transport in the transition between the two boundary states to be numerically investigated. (*b*) Coefficient of variance in the fast electron density at the target rear side in the simulation results, as a function of the magnitude of the resistivity peak.

intermediate $\eta - T$ profiles were then defined and used to enable the sensitivity of the fast electron transport pattern to this material property to be investigated.

3. Influence of the resistivity-temperature profile on the fast electron transport pattern

In this section we investigate the sensitivity of the fast electron beam transport pattern to both the magnitude of η and the shape of the $\eta - T$ profile. The electron beam parameters (as discussed above) are fixed throughout, and selected based on an example case of a 350 J, 1 ps laser pulse focused to produce a Gaussian spatial-intensity profile with full width at half maximum (FWHM) equal to 7 μm, and thus a peak intensity of $\sim 5 \times 10^{20}$ Wcm^{-2}. These pulse parameters are routinely available experimentally on the Vulcan laser at the Rutherford Appleton Laboratory and similar parameters are achievable at several other petawatt-class high power laser facilities.

3.1. Onset of beam filamentation in lithium

We choose lithium as a case study material for several reasons. Firstly, the overall shape of the $\eta - T$ profile is characteristic of a metallic target; η is low at room temperature, increases as a function of T by several orders of magnitude to a maximum value, and then decreases rapidly with further increases in T. The low-temperature increase in η is driven by changes to the electron collision frequency. The peak arises due to the minimum scattering length in the plasma, and the decrease at high temperatures arises due to the decrease in the Coulomb cross section with increasing electron velocity corresponding to the Spitzer regime. Secondly, the η-peak occurs at low temperatures (~ 5–15 eV), compared to higher Z metals, and its position and magnitude vary significantly with the degree of lattice disorder.

As shown in figure 1(*a*), η has a peak value of 1.6×10^{-6} Ωm at $T = 15$ eV for the case of an ordered lattice (Li case A), and increases to 4.2×10^{-6} Ωm at $T = 5$ eV for the case of

disordered lithium (Li case G). The increase in η is caused by a decrease in the electron mean free path as the degree of ionic lattice order decreases. As discussed above, a number of intermediate devised profiles, corresponding to cases B–F in figure 1(*a*), are also modelled to investigate the transition between the ordered and disordered cases.

Figure 2 shows simulation results for four example cases of fast electron transport in Li targets with increasing degree of lattice disorder: (*a*) case A (i.e. ordered Li); (*b*) case D; (*c*) case E; and (*d*) case G (i.e. fully disordered Li). The top row shows the B_z component of the resistive magnetic field, and the middle and bottom rows show the fast electron density in the *X-Y* (mid-plane) and *Y-Z* (rear side) planes, respectively, after an example simulation time of 1.4 ps. The arc shape at $X = 80$–120 μm in figure 2(*e*)–(*h*) corresponds to the rear of the fast electron distribution undergoing spherical expansion within the cone with half-angle equal to 50°. The position of this feature moves with time as defined by the fast electron velocity.

A transition from a relatively smooth fast electron beam profile in the case of ordered Li, to a strongly filamented beam for disordered Li, is observed. The percentage variance in the electron beam density over a sample area corresponding to 30% of the total beam area (centred on the beam axis, $Y = Z = 0$) is shown in figure 1(*b*). There is a clear positive correlation between the degree of disorder in the beam and the magnitude of the η-peak, which is consistent with the filamentation being caused by resistive instabilities (see for example reference [21]). The shift in temperature at which the peak occurs has little effect compared to the change in its magnitude. Thus the magnitude of the resistivity in the low-temperature transient WDM regime is shown to play an important role in the onset of resistive filamentation of the fast electron beam.

3.2. Annular fast electron transport in silicon

Next we consider the case of silicon, which has a distinctly different $\eta - T$ profile, as reported in reference [12]. Si is a
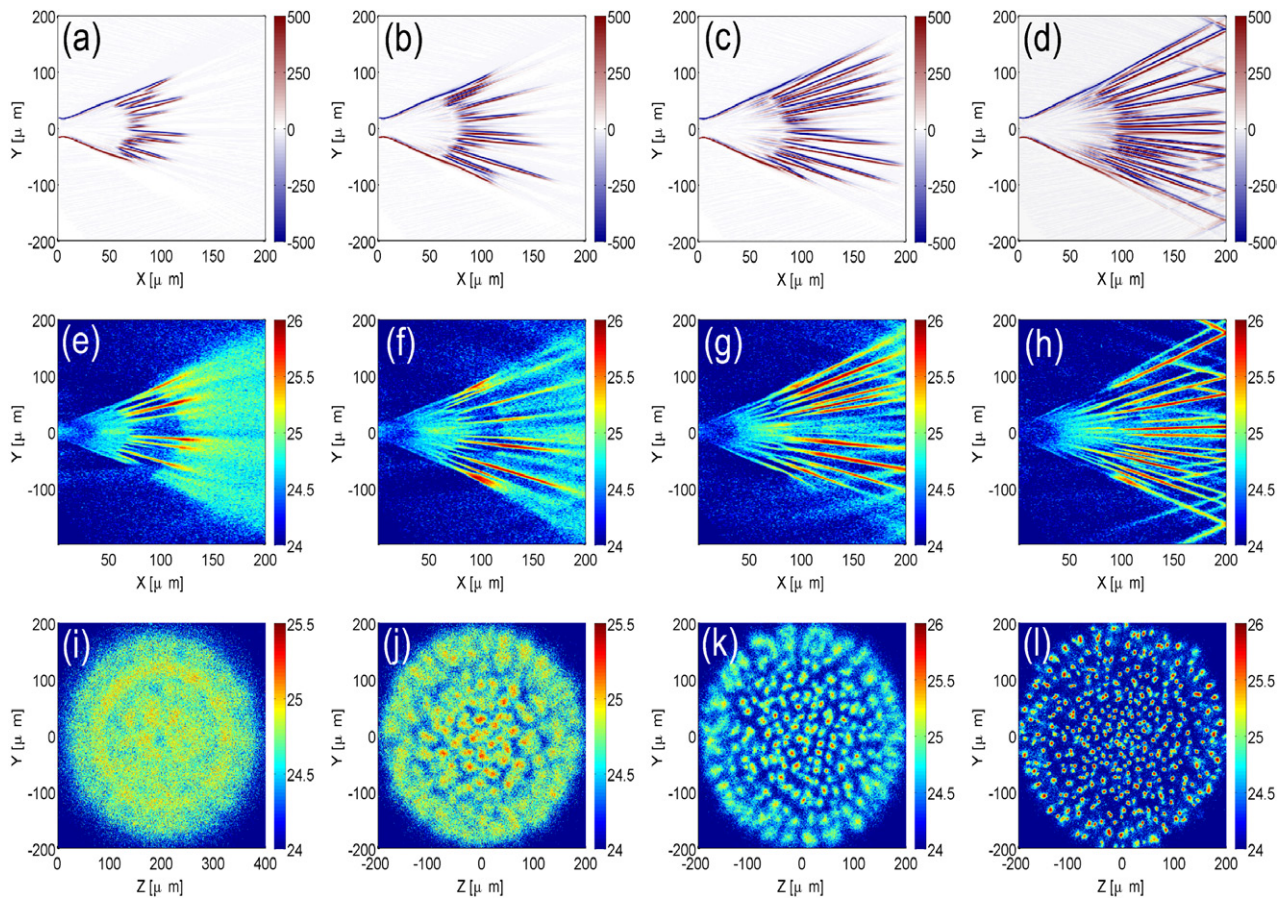
Figure 2. Hybrid-PIC simulation results, 1.4 ps after the start of the electron injection, showing: top row: [*X-Y*] mid-plane 2D maps of the magnetic flux density (B_z component in Tesla) for (*a*) case A; (*b*) case D; (*c*) case E, and (*d*) case G; middle row: corresponding results showing $\log_{10}$ fast electron density maps (m^{-3}), in the [*X-Y*] mid-plane; bottom row: corresponding results showing $\log_{10}$ fast electron density maps (m^{-3}), at the rear-surface [*Y-Z*] plane ($X = 200\ \mu m$).

semiconductor and therefore the initial η at room temperature is relatively high. However, as shown in figure 3(*a*), in the case of an ordered lattice structure (case A), η decreases sharply due to excitation of electrons above the band gap, before increasing again to a peak value at $T \approx 50$ eV as electrons are scattered more frequently, and finally decreasing at higher T in the Spitzer regime due to the decrease in the collision cross section. It was first shown in MacLellan *et al* [12] that the dip in η at a few eV leads to a reversal in the resistivity gradient, $\nabla\eta$, near the edges of the fast electron beam where the target is heated to relatively low temperatures. This in turn produces a reversal in the direction of the self-generated resistive B-field, due to the $\nabla\eta \times \mathbf{j}_f$ term in the field growth rate. The azimuthal field enveloping the beam acts to pinch it, whereas this reversed field forces electrons towards the beam edge. Together these field components act to channel fast electrons into an annular pattern, driving a localised increase in the fast electron beam density in the resulting ring. The temperature in this localised region rapidly increases (resistive heating scales as $\mathbf{j}_f^2$), driving down the resistivity, which reinforces the annular profile as the fast electrons propagate across the remainder of the target. Here, we investigate the sensitivity of the annular transport pattern to: (1) the magnitude of η in the low temperature dip; and (2) the temperature at which the dip occurs.

Figure 3(*a*) shows the $\eta - T$ profiles for ordered and highly disordered forms of silicon, as calculated from the QMD-Kubo–Greenwood approach—cases A and D, respectively. Cases B and C correspond to two intermediate devised profiles, effectively corresponding to differing degrees of lattice disorder. The fast electron transport patterns for all four cases are shown in figure 4.

The ordered lattice produces an annular transport pattern, as first reported in reference [12] for the same laser and electron beam parameters as used in the present study. As discussed in reference [22], the annular structure is sensitive to the laser pulse parameters. There is an optimum laser peak intensity range for transporting fast electrons within the ring. The annulus-to-axial electron density contrast ratio is also sensitive to the laser intensity, as this determines the relative strength of the resistive magnetic field components. To achieve the optimum annular profile, the hollowing component of the B-field should be high enough to deflect electrons into the annulus, but the collimating component should not be so high as to strongly collimate the beam. The radius of the ring is also shown to be sensitive to the laser focal spot size in reference [22].

The results in figure 4 indicate that with increasing η filamentation occurs at the centre of the beam, and for the fully disordered case (case D), the beam is completely filamented.
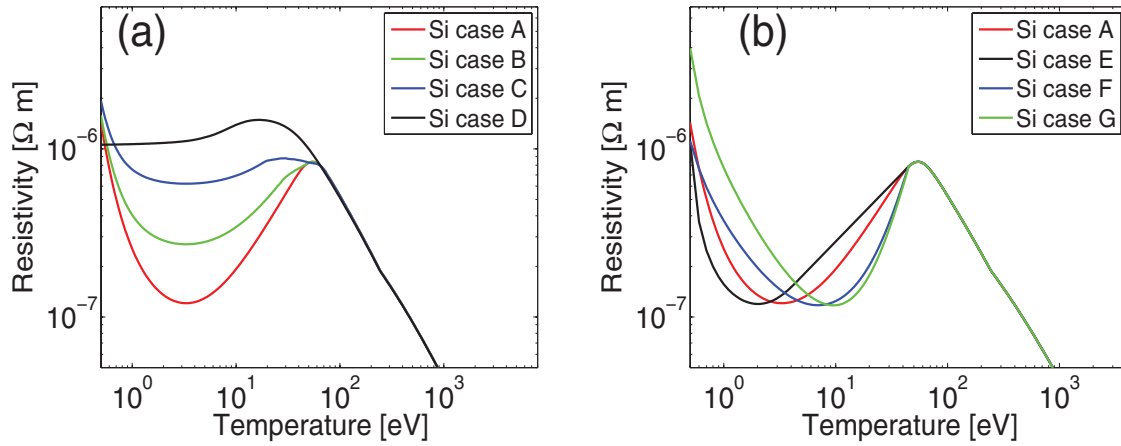
Figure 3. (*a*) Electrical resistivity of silicon as a function of target temperature for an ordered (case A) and a disordered (case D) ion array, based on *ab initio* QMD-Kubo–Greenwood calculations. Cases B and C correspond to intermediate devised $\eta - T$ profiles. (*b*) Cases E–G correspond to devised $\eta - T$ profiles for which the temperature at which the η-dip occurs is varied to enable investigation of the resulting effect on fast electron transport.
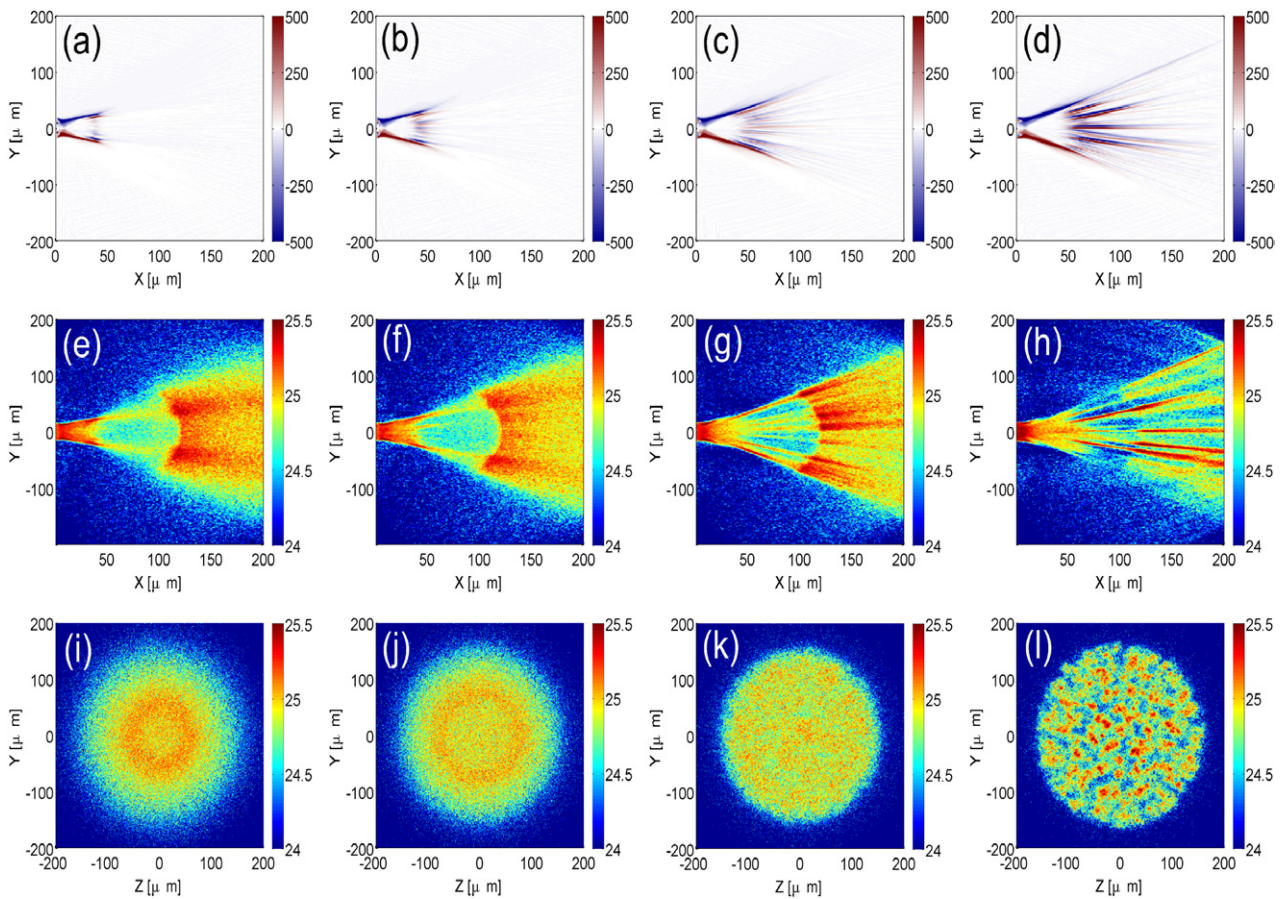

Figure 4. Caption as for figure 2, for (*a*) Si case A; (*b*) Si case B; (*c*) Si case C, and (*d*) Si case D. A transition from an annular to a filamented electron beam transport pattern is observed with decreasing degree of lattice order.

As was found for lithium, the value of η in the transient WDM regime has a defining effect on the fast electron transport pattern.

Next, the temperature at which the low-temperature η dip occurs is changed, as shown in figure 3(*b*). Case A again corresponds to the QMD-Kubo–Greenwood calculation for ordered silicon (used as the reference case) and cases E to G are devised profiles. The results of example hybrid-PIC simulations, for otherwise identical simulation parameters to the results for figure 4, are shown in figure 5. Moving the dip to higher temperature decreases the radius of the annular beam. Interrogation of the simulation results shows that this arises because the radius at which the reversal in the resistive B-field (which seeds the annular transport) occurs decreases with increasing background target temperature. The correlation between these two radii and the temperature at which the
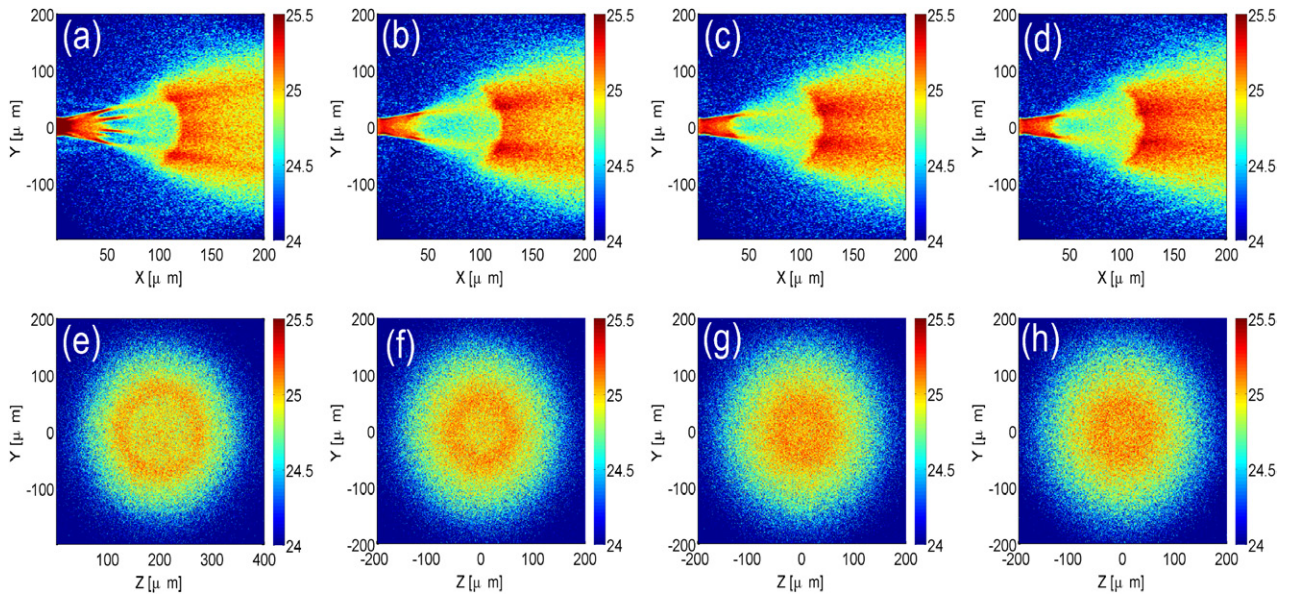
Figure 5. Log$_{10}$ fast electron density maps (m^{-3}), in the [*X-Y*] mid-plane and rear-surface [*Y-Z*] plane for (*a*) Si case E, (*b*) Si case A, (*c*) Si case F and (*d*) Si case G.

dip in resistivity occurs is shown in figure 6. The final size of the ring is found to be quite sensitive to the radius at which the annular transport is seeded and thus the temperature at which the resistivity gradient change occurs.

We note that in this parameter scan, in order to maintain a similar shape in the $\eta - T$ curve in the region of the dip, the magnitude of the resistivity at temperatures of the order of 1 eV increases as the temperature at which the dip occurs is increased. Due to the relatively small temperature range over which this η increase occurs it does not significantly influence the transport physics—a significant increase over a wider temperature range would result in beam filamentation, as discussed above.

Together with the Li results, these results clearly illustrate the sensitivity of the fast electron transport pattern to both the magnitude of the η and the shape of the $\eta - T$ profile in the WDM regime. These results highlight the potential to engineer a particular fast electron transport pattern by controlling the $\eta - T$ profile. This can be done by careful selection of target material and allotrope, or by doping a material to modify its resistivity profile.

4. Scaling to fast ignition laser drive parameters

We next briefly explore the potential for inducing annular fast electron transport with drive laser pulse parameters relevant to FI. A discussion of FI requirements and restrictions on laser drive parameters can be found in references [23, 24]. The requirements are determined by the compression and burn physics. Specifically, the optimum fast electron energy, intensity, pulse duration and hot spot radius are all dependent on the density of the compressed DT mass. A typical FI scenario could involve, for example, the DT fuel being compressed to achieve a peak density of the order of 300 g.cm^{-3}, dropping to a few g.cm^{-3} at the tip of a re-entrant cone [6]. A peak density of this order requires ~20 kJ of electron energy to
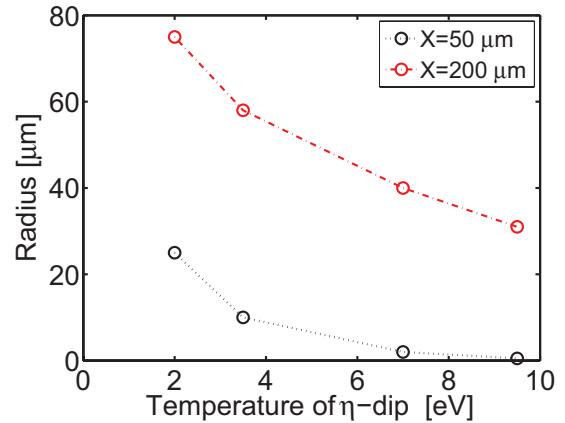

Figure 6. Radius of the annulus at the target rear side ($X = 200\ \mu m$) and at $X = 50\ \mu m$ (at which the reversal in the B-field occurs) as a function of the temperature of the centre of the η-dip.

be transported and deposited in a hot spot of ~20 μm-radius within a duration of ~20 ps (before fuel disassembly occurs). As discussed above, a key challenge for the successful realisation of FI is to reduce the drive laser energy requirements for a given set of DT plasma compression conditions.

The development of schemes to induce an annular fast electron beam transport pattern could play a key role in lowering the drive laser energy requirements. An annular beam profile can enable the propagation of an electron beam of higher current when compared to a uniform beam, as a consequence of the Alfvén limit increasing by a factor $r/\Delta r$, where r and Δr are the radius and width of the annulus, respectively [25]. In the context of FI, Davies [8] showed that the resistive decay of the return current, which can inhibit the propagation of the fast electron beam, can be compensated for by propagating the electron beam in an annular structure. Annular fast electron beam transport in solids can also be used to generate beams of MeV ions with an annular profile [12]. Temporal *et al* [26] shows that an annular beam of protons as the first of
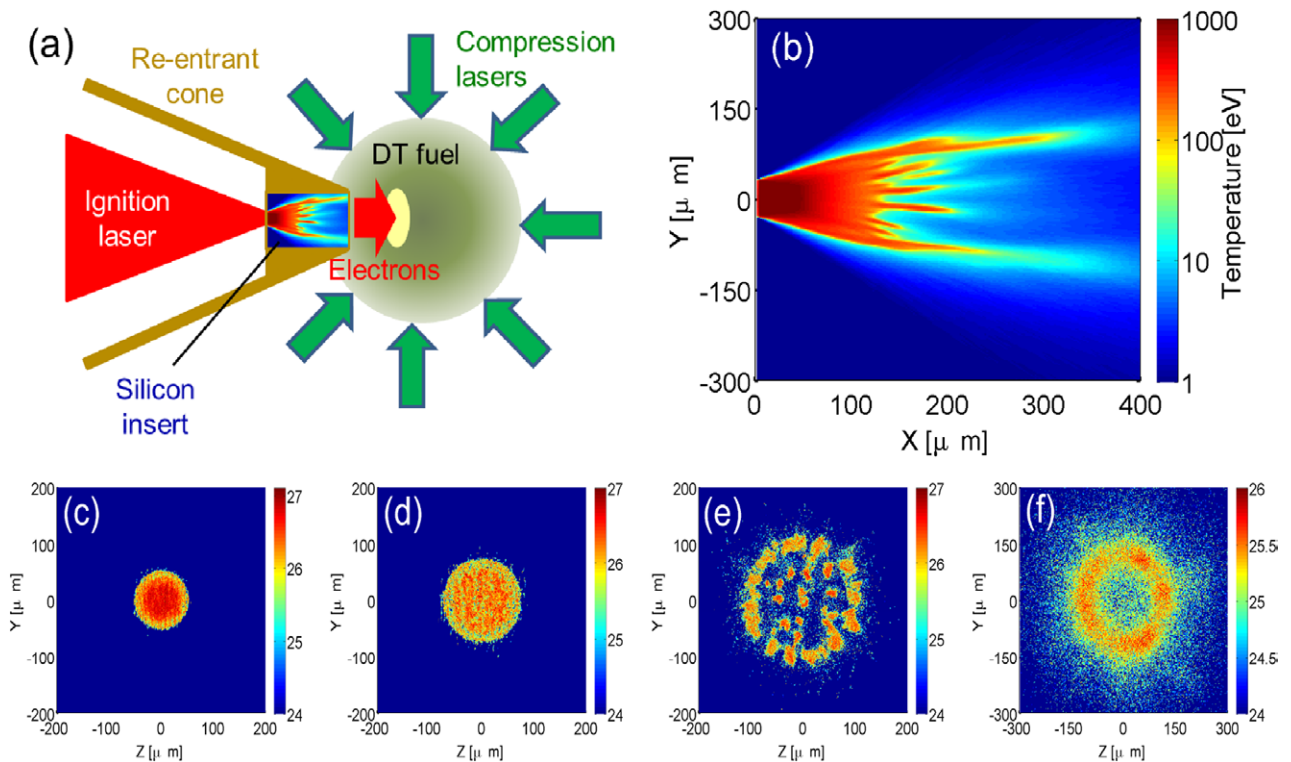
Figure 7. (*a*) Schematic illustrating a cone FI target scheme with a silicon insert to induce an annular fast electron beam transport pattern. (*b*) Background target temperature in the [*X-Y*] mid-plane for the $L = 400\ \mu$m case. (*c*)–(*f*): Log$_{10}$ fast electron density maps (m^{-3}) at the rear-surface [*Y-Z*] plane, for (*c*) $L = 50\ \mu$m; (*d*) $L = 100\ \mu$m; (*e*) $L = 200\ \mu$m; and (*f*) $L = 400\ \mu$m.

two ignition driver pulses could potentially be used to induce some additional radial compression of a localised region of the fuel, reducing the overall ignition energy requirements by a factor of almost two.

In order to seed an annular fast electron beam profile, a silicon insert could be used in advanced fusion target designs, for example near the tip of a hollow gold cone inserted into the fuel pellet, as shown schematically in figure 7(*a*). For a scheme such as this to work an engineering solution would need to be adopted to enable the silicon target to remain cold during the fuel compression stage. Nevertheless it is interesting to explore whether the annular beam transport physics explored in the preceding section is relevant when scaling up the laser pulse energy to ignition parameters. It should be noted that we are not assessing the total energy transported, nor investigating the annular beam propagation within the D–T fuel. Our exploration is limited to assessing whether an annular beam transport profile can be induced for FI laser pulse parameters.

We consider a total electron energy of 20 kJ (corresponding for example to an ignition laser pulse energy equal to 100 kJ and 20% conversion efficiency to fast electrons), a pulse duration equal to 20 ps and peak laser intensity equal to 4×10^{20} Wcm^{-2}. These drive parameters are typical for DT fuel compression to a peak density of ~300 g.cm^{-3}. A series of simulations were performed as a function of the thickness (propagation length), L, of the silicon sample. Example results are shown in figures 7(*c*)–(*f*) for $L = 50$–400 μm, 5 ps into the simulation. The output is selected at this time step to minimise the effects of lattice melt, which as the discussion above shows

will change the $\eta - T$ profile (the lattice melt time for silicon is experimentally measured to be of the order of 7–10 ps [27]). The corresponding target temperature map (in the [*X-Y*] mid-plane) is shown in figure 7(*b*) for the $L = 400\ \mu$m case.

It is clear from the example results in figures 7(*c*)–(*d*) that an annular fast electron beam is also induced at the high electron currents required for FI. However, the annular profile only emerges after a propagation length of 200–300 μm, at which depth the target temperature is low enough for low-temperature resistivity effects to play a significant role, as shown in figure 7(*b*). The thickness of the silicon insert within the cone would need to be of this order and furthermore be shielded from radiation produced in the fuel and surrounding environment in order for this scheme to work. The temperature (and thus resistivity) gradients required to induce the annular beam profile are driven by the dominant Ohmic heating mechanism. Secondary heating due to bremsstrahlung and x-ray radiation produced by the fast electrons within the silicon sample is not considered. In the case of sub-kJ energy laser pulses for which the annular transport profiles in silicon have been experimentally verified [12] radiation heating has little effect. However, the higher radiation flux produced in the case of FI-relevant pulses may influence the formation of these patterns and should be considered in a more detailed assessment of this scheme.

A further issue to consider is that the diameter of the annular beam in figure 7(*d*) is significantly larger than the optimum hot spot size, as determined for a Gaussian-beam profile. As discussed in reference [22], the ring size is tunable by variation of the laser drive, and thus electron source,

parameters. These parameters are however largely defined by the compression and ignition physics, and thus only variable over a relatively small range. Given that the width (Δr) of the annular profile is ~20 μm, the minimum electron beam size, corresponding to closure of the ring (as demonstrated in reference [22]) is ~40 μm. In this case the annular beam transport acts not to produce a distinct ring pattern, but simply to prevent the fast electron beam diverging. From the simulation results presented in the preceding section (figure 5), instead of changing the drive laser pulse parameters, a target material with a similar $\eta - T$ profile to silicon, but with the characteristic dip occurring at higher temperatures, could be used to produce an annular transport pattern with a smaller radius. As this resistivity dip arises due to excitation of electrons above the band gap in silicon at ~1.1 eV, a material with a larger band gap, but similar $\eta - T$ profile shape, such as diamond ($\sim$ 5.5 eV), may be suitable.

The purpose of this discussion is simply to establish whether in principle an annular fast electron beam could be produced for typical fast ignition laser drive parameters. A fuller investigation is required to determine the sensitivity to many other electron source parameters not considered here, e.g. the initial divergence of the injected electron beam. Furthermore, the precise requirements for fast ignition using annular electron or proton beams requires detailed numerical investigation of ignition physics, which is beyond the scope of the present study.

5. Conclusions

In conclusion, the effects of the $\eta - T$ profile at low temperature on resistive B-field generation, and thus the transport patterns of fast electrons in solids, has been investigated using a 3D hybrid-PIC code. The results demonstrate that the magnitude of the resistivity at temperatures in the transient WDM regime (1–10 eV) defines the resistive instability growth rate and thus the onset of fast electron beam filamentation. In the case of semiconductors, the electronic band gap results in a $\eta - T$ profile which includes a dip in η at an energy above the band gap energy, due to excitation into the conduction band. This change in the slope of the resistivity gradient gives rise to a reversal in B-field just inside the envelope of beam, where the temperature gradient is large, which acts together with a collimating azimuthal B-field to channel the fast electrons into an annular beam profile. The diameter of the ring is shown to be inversely proportional to the temperature at which the dip in low-temperature resistivity occurs. It is further shown that the onset of resistive instabilities in electron transport is sensitive to the degree of lattice melt occurring.

This study has a number of potential implications for fast ignition: (1) it demonstrates the importance of taking appropriate account of low-temperature resistivity in fast electron transport simulations, particularly when the objective is to compare the results with experimental data involving targets which are initially cold and typically with thickness larger then a few tens of microns—experiments of this type on existing high power laser facilities are used to benchmark modelling and code development for use in FI; (2) it shows the importance of considering the form or allotrope of a given material in the design of advanced fusion target schemes involving fast electrons; and (3) the brief exploration of the possibility to produce an annular fast electron beam by resistive-guiding for FI pulse parameters highlights the possibility to develop new schemes for FI involving annular fast electron beams.

References

[1] Daido H, Nishiuchi M and Pirozhkov A S 2012 *Rep. Prog. Phys.* **75** 056401
[2] Macchi A, Borghesi M and Passoni M 2013 *Rev. Mod. Phys.* **85** 751
[3] Perry M D *et al* 1999 *Rev. Sci. Instrum.* **70** 265
[4] Norreys P A *et al* 1999 *Phys. Plasmas* **6** 215
[5] Tabak M *et al* 1994 *Phys. Plasmas* **1** 1626
[6] Kodama R *et al* 2001 *Nature* **412** 798
[7] Wilks S C and Kruer W L 1997 *IEEE J. Quantum Electron.* **33** 1954
[8] Davies J R 2004 *Phys. Rev.* E **69** 065402
[9] Spitzer L and Harm R 1953 *Phys. Rev.* **89** 5
[10] McKenna P *et al* 2011 *Phys. Rev. Lett.* **106** 185004
[11] MacLellan D A *et al* 2013 *Laser Part. Beams* **31** 475–80
[12] MacLellan D A *et al* 2013 *Phys. Rev. Lett.* **111** 167588
[13] MacLellan D A *et al* 2014 *Phys. Rev. Lett.* **113** 185001
[14] Robinson A P L *et al* 2012 *Phys. Rev. Lett.* **108** 125004
[15] Bell A R and Kingham R J 2003 *Phys. Rev. Lett.* **91** 035003
[16] Bell A R *et al* 2006 *Plasma Phys. Control. Fusion.* **48** R37–57
[17] Thomas A G R *et al* 2012 *J. Comput. Phys.* **231** 1051
[18] Coury M *et al* 2013 *Phys. Plasmas* **20** 043104
[19] Desjarlais M P, Kress J D and Collins L A 2002 *Phys. Rev. E* **66** 025401
[20] Kresse G and Hafner J 1993 *Phys. Rev. B* **47** 558
[21] Gremillet L *et al* 2002 *Phys. Plasmas* **9** 941
[22] MacLellan D A *et al* 2014 *Plasma Phys. Control. Fusion* **56** 084002
[23] Atzeni S 1999 *Phys. Plasmas* **6** 3316
[24] Atzeni S, Schiavi A and Bellei C 2007 *Phys. Plasmas* **14** 052702
[25] Alfve H 1939 *Phys. Rev.* **55** 425
[26] Temporal M *et al* 2008 *Phys. Plasmas* **15** 052702
[27] Shank C V *et al* 1983 *Phys. Rev. Lett.* **50** 454